EUROPEAN ORGANIZATION FOR NUCLEAR RESEARCH (CERN)

Search for top squarks in the four-body decay mode with single lepton final states in proton-proton collisions at $\sqrt{s} = 13\,\text{TeV}$

The CMS Collaboration

Abstract

A search for the pair production of the lightest supersymmetric partner of the top quark, the top squark ($\widetilde{t}_1$), is presented. The search targets the four-body decay of the $\widetilde{t}_1$, which is preferred when the mass difference between the top squark and the lightest supersymmetric particle is smaller than the mass of the W boson. This decay mode consists of a bottom quark, two other fermions, and the lightest neutralino ($\widetilde{\chi}_1^0$), which is assumed to be the lightest supersymmetric particle. The data correspond to an integrated luminosity of $138\,\text{fb}^{-1}$ of proton-proton collisions at a center-of-mass energy of 13 TeV collected by the CMS experiment at the CERN LHC. Events are selected using the presence of a high-momentum jet, an electron or muon with low transverse momentum, and a significant missing transverse momentum. The signal is selected based on a multivariate approach that is optimized for the difference between $m(\widetilde{t}_1)$ and $m(\widetilde{\chi}_1^0)$. The contribution from leading background processes is estimated from data. No significant excess is observed above the expectation from standard model processes. The results of this search exclude top squarks at 95% confidence level for masses up to 480 and 700 GeV for $m(\widetilde{t}_1) - m(\widetilde{\chi}_1^0) = 10$ and 80 GeV, respectively.

Submitted to the Journal of High Energy Physics

1 Introduction

Supersymmetry (SUSY) [1–6] predicts the existence of a scalar partner for each left-handed and right-handed fermion of the standard model (SM). Searches for SUSY are among the important focal points of the physics program at the CERN LHC, since SUSY naturally solves the problem of quadratically divergent loop corrections to the mass of the Higgs boson [7–9]. If R parity [10] is conserved, supersymmetric particles would be produced in pairs, and their decay chains would end with the lightest supersymmetric particle (LSP), often considered to be the lightest neutralino $\widetilde{\chi}_1^0$. Such an LSP, being neutral, weakly interacting, and massive, would have the required characteristics for a dark matter particle, and thus, would offer a solution to another shortcoming of the SM. When the symmetry is broken, the scalar partners of an SM fermion acquire a mass different from the mass of the SM partner, with the mass splitting between scalar mass eigenstates being proportional to the mass of the SM fermion. Since the top quark is the heaviest fermion of the SM, the splitting between its chiral supersymmetric partners can be the largest among all supersymmetric quarks (squarks). The lighter supersymmetric scalar partner of the top quark, the top squark ($\widetilde{t}_1$), could therefore be the lightest squark. If SUSY is realized in nature, cosmological observations imply that the lightest top squark is almost degenerate with the LSP [11]. In this scenario, because the mass difference between the $\widetilde{t}_1$ and the $\widetilde{\chi}_1^0$ is smaller than the mass of the W boson, the two- and three-body decays of the $\widetilde{t}_1$ are kinematically forbidden, while the two-body decay to $c\widetilde{\chi}_1^0$ can be suppressed depending on the parameters of the model. This motivates the search for the four-body decay $\widetilde{t}_1 \to b f \bar{f}' \widetilde{\chi}_1^0$, where b stands for the bottom quark, and the fermions f and $\bar{f}'$ can be either quarks or leptons. Throughout this paper, charge conjugation is assumed. Figure 1 represents a simplified model [12–17] of the production of $\widetilde{t}_1 \bar{\widetilde{t}}_1$ in proton-proton (pp) collisions, where each $\widetilde{t}_1$ and $\bar{\widetilde{t}}_1$ undergoes a four-body decay.
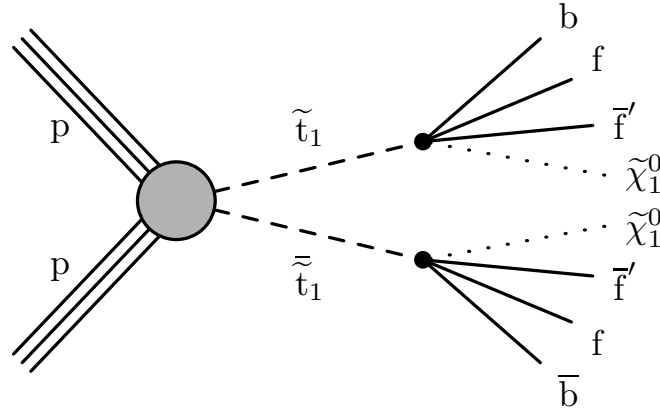

Figure 1: Diagram of top squark pair production $\widetilde{t}_1 \bar{\widetilde{t}}_1$ in pp collisions, with a four-body decay of each top squark.

In this paper we combine the previous 2016 result of CMS at $\sqrt{s} = 13\,\text{TeV}$ [18] with data recorded in 2017 and 2018. The results of 2016 are directly taken from Ref. [18], except the integrated luminosity and its uncertainty, which are updated to their latest values [19]. The total integrated luminosity for the combined 2016–2018 analysis is $138\,\text{fb}^{-1}$.

In the present search a final state is considered, where the fermions f and $\bar{f}'$ represent a charged lepton and its neutrino for the decay products of one $\widetilde{t}_1$, and two quarks for the other top squark. A 100% branching fraction is assumed for the four-body decay when interpreting

the results [12]. The considered final states contain at least one jet, a large missing transverse momentum, and exactly one charged lepton, which can be either an electron or a muon. The choice of final states where one top squark decays into a lepton is motivated by the decrease of the contributions from the multijet background in this mode, while increasing the selection efficiency with the other top squark decaying hadronically. The selected jet, attributed to initial-state radiation (ISR) of a parton, is required to have high transverse momentum (p_T). Both neutralinos and the neutrino escape undetected, leaving high missing transverse momentum. Electrons and muons can be efficiently reconstructed and identified with p_T as low as 5.0 and 3.5 GeV, respectively. The signal selection is based on a multivariate analysis, followed by a counting experiment. This approach takes advantage of the different correlations between the discriminating variables for signal and background, and is adapted for different $\Delta m = m(\widetilde{t}_1) - m(\widetilde{\chi}_1^0)$ kinematic regions, thus enhancing the reach of the search across the $(m(\widetilde{t}_1), m(\widetilde{\chi}_1^0))$ space. The main contributions to the background events are W+jets, $t\bar{t}$, and Z+jets processes, and are predicted from data. A search in the single-lepton final state for the four-body decays of the $\widetilde{t}_1$ has been performed by the ATLAS Collaboration at $\sqrt{s} = 13$ TeV [20], and a comparison of its results to the present search is provided in this paper. Tabulated results are provided in the HEPData record for this search [21].

2 The CMS detector

The central feature of the CMS apparatus [22] is a superconducting solenoid of 6 m internal diameter, providing a magnetic field of 3.8 T. Within the solenoid volume are a silicon pixel and strip tracker, a lead tungstate crystal electromagnetic calorimeter (ECAL), and a brass and scintillator hadron calorimeter (HCAL), each composed of a barrel and two endcap sections. Forward calorimeters extend the pseudorapidity coverage provided by the barrel and endcap detectors. The silicon tracker measures charged particles within the pseudorapidity range $|\eta| < 2.5$. Muons are detected in gas-ionization chambers embedded in the steel flux-return yoke outside the solenoid. It is a multipurpose, nearly hermetic detector, designed to trigger on [23, 24] and identify electrons, muons, photons, and hadrons [25–27].

3 Data and simulated samples

The search described in this paper is performed using data from pp collisions recorded in 2017–2018 by the CMS experiment at the LHC at a center-of-mass energy of 13 TeV. These results are statistically combined with the result from the search using the data of 2016, corresponding to an integrated luminosity of 36.3 fb^{-1} that was updated for this paper. The 2017 and 2018 data samples correspond to an integrated luminosity of 41.5 fb^{-1} and 59.8 fb^{-1}, respectively, bringing the total integrated luminosity for the combined 2016–2018 analysis to 138 fb^{-1}.

Signal and background processes are simulated using several Monte Carlo (MC) event generators. The SM background MC samples are used to estimate the relation between the control and signal regions for the main background processes, to validate the background estimation methods based on control samples in data, and finally, to predict the contributions from rare processes. The W+jets and $Z \rightarrow \nu\bar{\nu}$+jets processes are generated at leading order (LO) by MADGRAPH5_aMC@NLO 2.4.2 [28]. The $t\bar{t}$ process is generated at next-to-leading order (NLO) by MADGRAPH5_aMC@NLO. The POWHEG v2.0 [29–36] generators are used for the NLO simulations of single top and associated tW production. Diboson events are simulated at NLO with MADGRAPH5_aMC@NLO and POWHEG. The LO (NLO) NNPDF3.1LO (NNPDF3.1NNLO) [37] parton distribution functions are used consistently with the order of the matrix element cal-

culation in the generated events. Additional rare backgrounds such as $t\bar{t}$ produced in association with a Z boson, W boson, or photon, referred to as $t\bar{t}X$, are generated with MAD-GRAPH5_aMC@NLO at NLO [38]. Hadronization and showering of events in all generated samples are simulated using PYTHIA 8.230 [39] with the CP5 tune [40] for the underlying event. All SM MC events are passed through a full simulation of the CMS apparatus, where the response of the detector is modeled using the GEANT4 [41] software. Generated events are processed using the same version of the CMS event reconstruction software used as for data. Additional pp collisions in the same or nearby beam crossings (pileup) are simulated and overlaid on the main pp interaction in the MC samples, with distributions that reproduce the conditions observed year-to-year in data. For the pair production of top squarks $(\tilde{t}_1\bar{\tilde{t}}_1)$, simulated samples are produced for $250 < m(\tilde{t}_1) < 800\,\text{GeV}$ in steps of $25\,\text{GeV}$, and $10 < \Delta m < 80\,\text{GeV}$ in steps of $10\,\text{GeV}$. The cross section for $\tilde{t}_1\bar{\tilde{t}}_1$ production, calculated using PROSPINO v.2 [42–48], is computed at next-to-next-to-leading-order (NNLO) accuracy, and includes next-to-next-to-leading-logarithmic (NNLL) corrections. This cross section varies between approximately 20 and 0.1 pb as $m(\tilde{t}_1)$ goes from 250 to 800 GeV. The generation of signal events with up to two additional jets, which can originate from ISR, is performed with MADGRAPH5_aMC@NLO and then interfaced with PYTHIA for the decay hadronization and showering. The modeling of the detector response for the signal is done with the CMS fast simulation program [49, 50].

Both signal and background simulated samples are corrected to account for discrepancies from data. Control regions (CRs) in data are used to measure the reconstruction efficiencies of leptons and jets produced by the hadronization of b quarks, "b jets", as well as the b jet misidentification probabilities for light-quark and gluon jets. The corrections are applied as a function of the p_T and η of the objects. Fast simulation signal samples are additionally corrected to take into account any potential difference with respect to the GEANT4 modeling. The latter corrections translate into efficiencies applied to b jets, leptons, and the modeling of the missing transverse momentum. The simulations of W+jets, $t\bar{t}$, and signal processes are corrected for the effect of ISR. The modeling of ISR for these processes is checked in data-based control samples that are highly enriched in $t\bar{t}$ or W+jets events. The simulation of $t\bar{t}$ events is tested by comparing the jet multiplicity observed in a control sample with the simulation, and the $t\bar{t}$ and signal samples are reweighted based on this comparison. The simulation of W+jets events is corrected based on the distribution of the sum of the magnitudes of the lepton ℓ transverse momentum $p_T(\ell)$ and the missing transverse momentum in a control sample.

4 Event reconstruction and object selection

Data and simulated events are reconstructed using the CMS particle-flow (PF) algorithm [51], which matches the information from all CMS subdetectors in order to describe the event in terms of global physics objects. These objects are denoted as PF candidates and are classified into mutually exclusive categories: electrons, muons, photons, and charged and neutral hadrons. The primary vertex (PV) is taken to be the vertex corresponding to the hardest scattering in the event, evaluated using tracking information alone, as described in Section 9.4.1 of Ref. [52].

Jets are reconstructed by applying the anti-k_T clustering algorithm [53, 54] to PF candidates with a distance parameter of 0.4. The pileup contribution to the jet momentum is partially taken into account by excluding the charged hadrons originating from vertices other than the PV from the jet-clustering algorithm. To account for pileup contributions from neutral particles and any inhomogeneity in the detector response, the jet p_T is further calibrated as described in Ref. [55]. Jets are required to satisfy $p_T > 30\,\text{GeV}$, and $|\eta| < 2.4$. The tagging of b jets (b tagging)

is performed with the DeepCSV algorithm [56] that uses information from the secondary vertex and is based on a deep neural network, with the standard medium working point described in Ref. [57]. The loose and tight working points of this algorithm, used only to define the W+jets and $t\bar{t}$ CRs, have a probability of about 10% and 0.1%, respectively, to misidentify light-flavor quark and gluon jets as b jets [57].

The missing transverse momentum vector, $\vec{p}_T^{\text{miss}}$, is computed as the negative vector $\vec{p}_T$ sum of all PF candidates in the event, and its magnitude is p_T^{miss}. The calibrations associated with the jet energy estimations are propagated to the $\vec{p}_T^{\text{miss}}$ [58].

Electron candidates are reconstructed from energy deposits in the ECAL and matched charged particle tracks in the inner tracker obtained using the Gaussian sum filter algorithm [25]. To reduce the number of misidentified electrons, additional constraints on the shape of the electromagnetic shower in the ECAL, the quality of the match between the trajectory of the track, and the ECAL energy deposit around the electron, and the relative HCAL deposit in the electron direction are applied. Electrons are required to have p_T above 5 GeV and $|\eta| < 2.5$, with a veto on electron candidates in the ECAL gap region $(1.4442 < |\eta| < 1.5660)$. They are identified with requirements on the observables that describe the matching of the measurements in the tracker and the ECAL, the description of energy clusters in the ECAL, and the amount of bremsstrahlung radiation emitted during the propagation through the detector. A loose working point of this algorithm is required for electrons to be selected, which has an average efficiency of 90%.

Muon candidates are reconstructed by combining the information from the silicon tracking systems and the muon spectrometer in a global fit [26] that assigns a quality to the matching between the tracker and muon systems and imposes minimal requirements on the track to reduce the misidentification of muons. The medium working point of this algorithm is required for muons to be selected, which ensures an efficiency above 98%. Muons are required to pass the selection requirements of $p_T > 3.5$ GeV and $|\eta| < 2.4$.

To select electrons or muons originating from the PV, the point of closest approach of the associated track with respect to the PV is required to have a transverse distance $|d_{xy}| < 0.02$ cm, and a longitudinal distance $|d_z| < 0.1$ cm. We define a lepton as being nonprompt either when it does not originate from the PV, or when a jet is misidentified as a lepton. Background processes with nonprompt leptons are one of the main contributions to the SM background in the signal regions. In this analysis, nonprompt leptons mostly arise from heavy-quark decays in jets produced in association with a $Z \rightarrow \nu\bar{\nu}$+jets decay, from multijet production, or from W+jets and $t\bar{t}$ events where the prompt lepton was not reconstructed and a different one was accepted. In order to suppress these types of processes, a requirement on the lepton isolation is applied, which uses a combination of an absolute and a relative isolation variable. The absolute isolation variable I_{abs} of the lepton is defined as the scalar sum of the p_T of PF candidates within a cone size of $R \equiv \sqrt{(\Delta\phi)^2 + (\Delta\eta)^2} = 0.3$, where ϕ is the azimuthal angle, around the lepton candidate, which is excluded from the sum, as are charged PF candidates not associated with the PV. The contributions from neutral particles originating from pileup are estimated according to the method described in Refs. [59, 60], and are subtracted from I_{abs}. The ratio of the lepton I_{abs} to the lepton p_T is defined as the lepton relative isolation I_{rel}. A uniform lepton selection efficiency as a function of p_T is achieved by requiring leptons to have $I_{\text{abs}} < 5$ GeV for $p_T(\ell) < 25$ GeV and $I_{\text{rel}} < 0.2$ for $p_T(\ell) \geq 25$ GeV.

5 Event selection

The data events collected by the trigger system are required to have both p_T^{miss} and H_T^{miss} above 120 GeV, where H_T^{miss} is the magnitude of the missing transverse momentum calculated only from jets. In order to maintain the performance of the online selection with increased luminosity from the late runs of 2017 onward, the condition $H_T > 60$ GeV is also required, where H_T is defined as the scalar p_T sum of all jets in the event. The efficiency of the combined p_T^{miss} and H_T^{miss} trigger is measured using an independent event sample with single-electron triggers and p_T thresholds of 35 and 32 GeV for the 2017 and 2018 data-taking periods, respectively.

The offline event selection is a two-step process. First, a preselection is applied to reduce the contribution of the main background processes (Section 5.1) by selecting a single charged lepton, large p_T^{miss}, and jets. Then, boosted decision trees (BDTs) [61, 62] are trained and used to define the signal selection (Section 5.2). The preselection is constructed to be as inclusive as possible in order to maintain a high signal efficiency for all Δm values, leaving the main selection to the BDT.

5.1 Preselection

The value of the preselection p_T^{miss} threshold is set close to the beginning of the maximum efficiency plateau of the combined p_T^{miss} and H_T^{miss} trigger, while optimizing the separation between signal and background performed by the BDTs. Events with $p_T^{miss} > 280$ GeV are selected, favoring the signal where two $\widetilde{\chi}_1^0$'s escape detection and where the p_T^{miss} is therefore larger than for SM processes. For these events, the trigger efficiency is above 98% for both years. To account for the small inefficiency, simulated samples are reweighted as a function of p_T^{miss} to match the p_T^{miss} distribution in data.

To suppress the contribution of SM processes, additional requirements are imposed on the selected events. In particular, to reduce the W+jets background, we require $H_T > 200$ GeV. To select the single-lepton topology, we demand exactly one identified electron or muon in the event, along with at least one jet. This selection reduces the contribution from the dilepton topology of $t\bar{t}$ events. To further improve the selection of signal over SM background events, at least one jet must have $p_T > 110$ GeV. These requirements are geared towards signal events in which the $\widetilde{t}_1\bar{\widetilde{t}}_1$ system recoils against a high-momentum ISR jet, Lorentz boosting the $\widetilde{\chi}_1^0$ and increasing p_T^{miss}. The ISR jet will often be the highest momentum (leading) jet in these events, and the leading-jet p_T threshold value is optimized in the same manner as for p_T^{miss}. Lastly, in events with at least two jets, the azimuthal angle between the directions of the leading and second-highest-p_T (subleading) jets must be smaller than 2.5 radians, suppressing the SM multijet background.

After the preselection, the W+jets and $t\bar{t}$ processes are the main SM backgrounds, making up about 70 and 20%, respectively, of the total expected background. The $Z \rightarrow \nu\bar{\nu}$+jets process contributes to the SM background by having jets, genuine p_T^{miss}, and a jet misidentified as a lepton. The remaining background processes are diboson, single top quark, Drell–Yan (DY), multijet, and $t\bar{t}X$ production where X is a vector boson. These processes are a less-important part of the expected background because of having a smaller cross section, a lower acceptance, or both. The $p_T(\ell)$, p_T^{miss}, and N_{jet} distributions after the preselection from the 2017 and 2018 data and the simulations are shown in Fig. 2, where N_{jet} is the number of jets in the event satisfying the jet criteria. The simulated background distributions for each year are normalized to the corresponding integrated luminosity. The level of agreement with data gives us confidence in training the BDTs with the simulated distributions for the second step in the event selection.
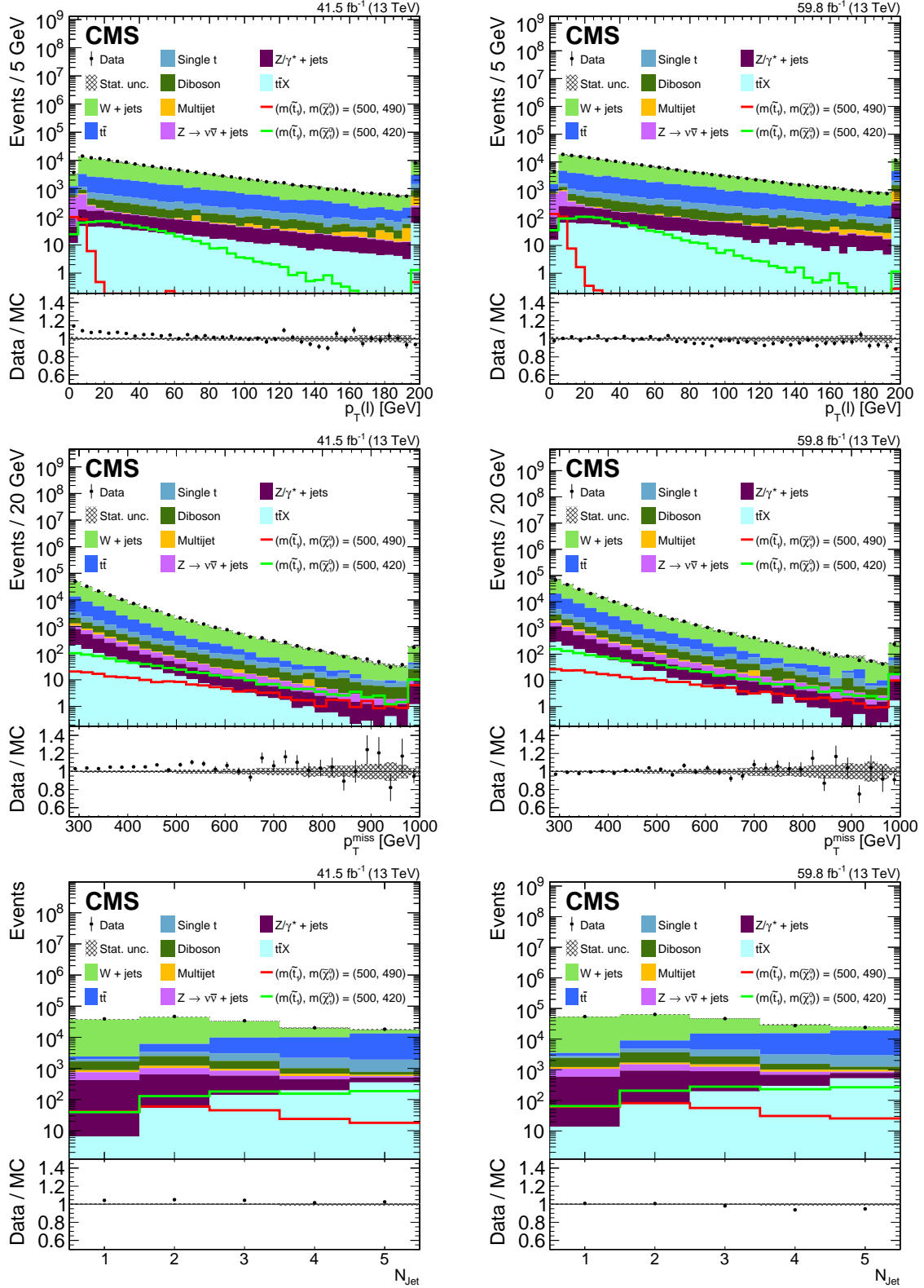
Figure 2: Distributions of $p_T(\ell)$ (upper), p_T^{miss} (middle), and N_{jet} (lower), after the preselection from 2017 (left) and 2018 (right) data (points) and simulation (colored histograms). The simulated distribution of two signal points are represented by colored lines, while not being stacked on the background distributions: $(m(\widetilde{t}_1), m(\widetilde{\chi}_1^0)) = (500, 490)$ and $(500, 420)$ GeV. The last bin in each plot includes the overflow events. The lower panels show the ratio of data to the sum of the simulated SM backgrounds. The shaded bands indicate the statistical uncertainty in the simulation predictions.

5.2 Classification and final selection

The selection of the signal events is based on a BDT [62] to take advantage of the different correlations among the discriminating variables for the signal and background processes. For each event passing the preselection, the BDT discriminator value, henceforth referred to as the BDT output, is evaluated. If the discriminator value exceeds the determined threshold, the event is retained. The choice of the discriminating variables used as input to the BDT is made by maximizing a figure of merit (FOM) [63] that takes into account the statistical and systematic uncertainties in a selection. Various BDTs are trained with different sets of discriminating variables, and a variable is included in the final set only if it significantly increases the FOM obtained for any selection using the BDT output. The list of the twelve retained input variables and a short description of their signal and background distributions is as follows:

- Variables related to p_T^{miss}: p_T^{miss} and m_T, where m_T is the transverse mass of the lepton + $\vec{p}_T^{\,miss}$ system, defined as: $m_T = \sqrt{2p_T^\mu p_T^{miss}[1 - \cos(\Delta\phi_{\mu,\vec{p}_T^{miss}})]}$, where $\Delta\phi$ is the azimuthal angular difference between the lepton $\vec{p}_T$ and $\vec{p}_T^{\,miss}$. The p_T^{miss} distribution extends to higher values for the signal than for the backgrounds due to the two undetected LSPs in the signal decays. The m_T spectrum peaks around 80 GeV for the SM background and is a broad distribution for the signal.

- Lepton-related variables: $p_T(\ell)$, $\eta(\ell)$, and $Q(\ell)$. The correlations between p_T^{miss} and $p_T(\ell)$ are different for the signal, where p_T^{miss} comes from three undetected particles (two $\widetilde{\chi}_1^0$ and a ν), than for W+jets and $t\bar{t}$ backgrounds, where p_T^{miss} is the result of a single undetected particle (ν). Because the decay products of the signal are more centrally produced than those of the W+jets process, the lepton pseudorapidity $\eta(\ell)$ distribution is populated at more central values for the signal than this background. The lepton charge $Q(\ell)$ is a discriminating variable because W^+ and W^- bosons are not produced equally at the LHC, while the signal events contain equal numbers of positively and negatively charged leptons.

- Jet-related variables: $p_T(ISR)$, $p_T(b)$, N_{jet}, and H_T. The variable $p_T(ISR)$ is defined as the p_T of the leading jet, and selects the high-momentum ISR jet in signal events. The $p_T(b)$ variable is the transverse momentum of the b-tagged jet with the highest b tagging discriminant value. Both the $p_T(ISR)$ and $p_T(b)$ variables are sensitive to the available phase space, which depends on $m(\widetilde{t}_1) - m(\widetilde{\chi}_1^0)$ for the signal, and $m(t) - m(W)$ for the $t\bar{t}$ background. The N_{jet} variable is sensitive to the mass difference Δm, while the H_T variable provides discrimination between signal and both the W+jets and $t\bar{t}$ backgrounds.

- b-jet-related variables: $N(b^{loose})$, $\Delta R(\ell,b)$, and $D(b)$. The number of loosely b-tagged jets $N(b^{loose})$, the distance in (η, ϕ) space between the directions of the lepton and the jet with the highest b tagging discriminant $\Delta R(\ell,b)$, and the highest b tagging discriminant per event $D(b)$ are included as input variables. While the preselection has no requirement on b tagging, information related to it is passed to the BDT to help discriminate between the signal and mainly the W+jets background.

The five most discriminating variables, in decreasing power, are $p_T(\ell)$, p_T^{miss}, $p_T(ISR)$, H_T, and m_T.

The discrimination power of the input variables varies as a function of Δm, as illustrated in Fig. 3 (left). An important feature of this search is the adaptation of the selection tool to the evolving kinematic variables of the signal over the $(m(\widetilde{t}_1), m(\widetilde{\chi}_1^0))$ plane. Therefore, this plane is divided into eight Δm regions (from 10 to 80 GeV, in steps of 10), and a separate BDT is trained

for each Δm region. The W+jets and $t\bar{t}$ processes, which constitute a large fraction of the total background after preselection, are included in the training of the BDT. This is done using both simulated signal and background events. The SM background samples are normalized to their theoretical cross sections in the training. As seen in Fig. 3 (right), different signal points with the same Δm have similar input variable distributions. This is expected since with the same Δm they have the same available phase space. Because of this, we group all the signal points with the same Δm together when training the BDT, thus increasing the number of signal events for each training. Because of the large variation of the $p_{\mathrm{T}}(\ell)$ spectrum across the $(m(\widetilde{t}_1),\ m(\widetilde{\chi}_1^0))$ plane, we require $p_{\mathrm{T}}(\ell) < 30\,\mathrm{GeV}$ for signal points with $\Delta m < 70\,\mathrm{GeV}$ before training the BDTs, while imposing no restriction on $p_{\mathrm{T}}(\ell)$ for signal points with higher Δm. This improves the ability of the BDT to separate the signal from the $t\bar{t}$ background.

The BDT output distributions for data and simulated SM background are shown in Figs. 4 and 5 for the 2017 and 2018 data, respectively. In each case a $(m(\widetilde{t}_1),\ m(\widetilde{\chi}_1^0))$ signal point belonging to the Δm value for which the training has been done is also reported. The BDT output is found to be different for various values of Δm, which is to be expected because of the changing mix of signal and background and the varying correlations across the $(m(\widetilde{t}_1),\ m(\widetilde{\chi}_1^0))$ plane, resulting in different BDT outputs for different Δm values. A good agreement between the data and simulation is observed for the BDT output distributions over the entire range, for all trainings; the region at small BDT output values (e.g., <0.3) is dominated by background events.

To check the validity of the BDT output in regions depleted in signal, we define a set of validation regions (VRs). These regions are chosen to be kinematically close but nonoverlapping with the region selected by the preselection, while using the same online selection. The first VR uses the preselection requirements discussed in Section 5.1, but where we require $200 < p_{\mathrm{T}}^{\mathrm{miss}} < 280\,\mathrm{GeV}$. This VR is used to validate the BDT output for all the trained BDTs. The second VR also uses the preselection requirements, but where we require $p_{\mathrm{T}}(\ell) > 30\,\mathrm{GeV}$. It is used for the validation of BDTs trained for signals with $\Delta m < 70\,\mathrm{GeV}$. This region is not used for BDTs trained for signals with $\Delta m = 70$ or $80\,\mathrm{GeV}$ because the entire range of the $p_{\mathrm{T}}(\ell)$ distribution is considered at preselection. The BDT output distributions for these VRs from data are consistent with those from the simulation. As described in Section 6, these VRs are also used to evaluate the uncertainty in the background determination.

A signal region (SR) is defined by requiring a lower limit on each BDT output. This limit is determined by minimizing the expected upper limit on the signal cross section of a benchmark $(m(\widetilde{t}_1),\ m(\widetilde{\chi}_1^0))$ signal point at the exclusion limit of the 2016 search. This choice implies that the benchmark signal points for the search from 2017 and 2018 data are at higher $\widetilde{t}_1$ and $\widetilde{\chi}_1^0$ masses than for the 2016 search. The exact values of the BDT selection requirements are reported in Table 2. As an illustration of the selection power of the BDT, in the case of $\Delta m = 80\,\mathrm{GeV}$, the SM background is suppressed by a factor of $\approx 3.7 \times 10^3$ compared to the preselection, while the signal is only reduced by a factor of ≈ 13.

6 Background estimation

The main background processes in this search are W+jets and $t\bar{t}$ with a prompt lepton, and events having a nonprompt lepton that passes the lepton criteria. We label the latter category nonprompt background. Nonprompt leptons mostly arise from the decay of heavy-flavor quarks and from misidentified hadrons. The processes contributing to the nonprompt background are mainly $Z \to \nu\bar{\nu}$+jets, and to a lesser extent, W+jets and $t\bar{t}$, where a jet is misidentified as a lepton. Furthermore, there can also be events in which a genuine lepton (mainly from W+jets or $t\bar{t}$) escapes detection, while a nonprompt lepton is selected. These three main
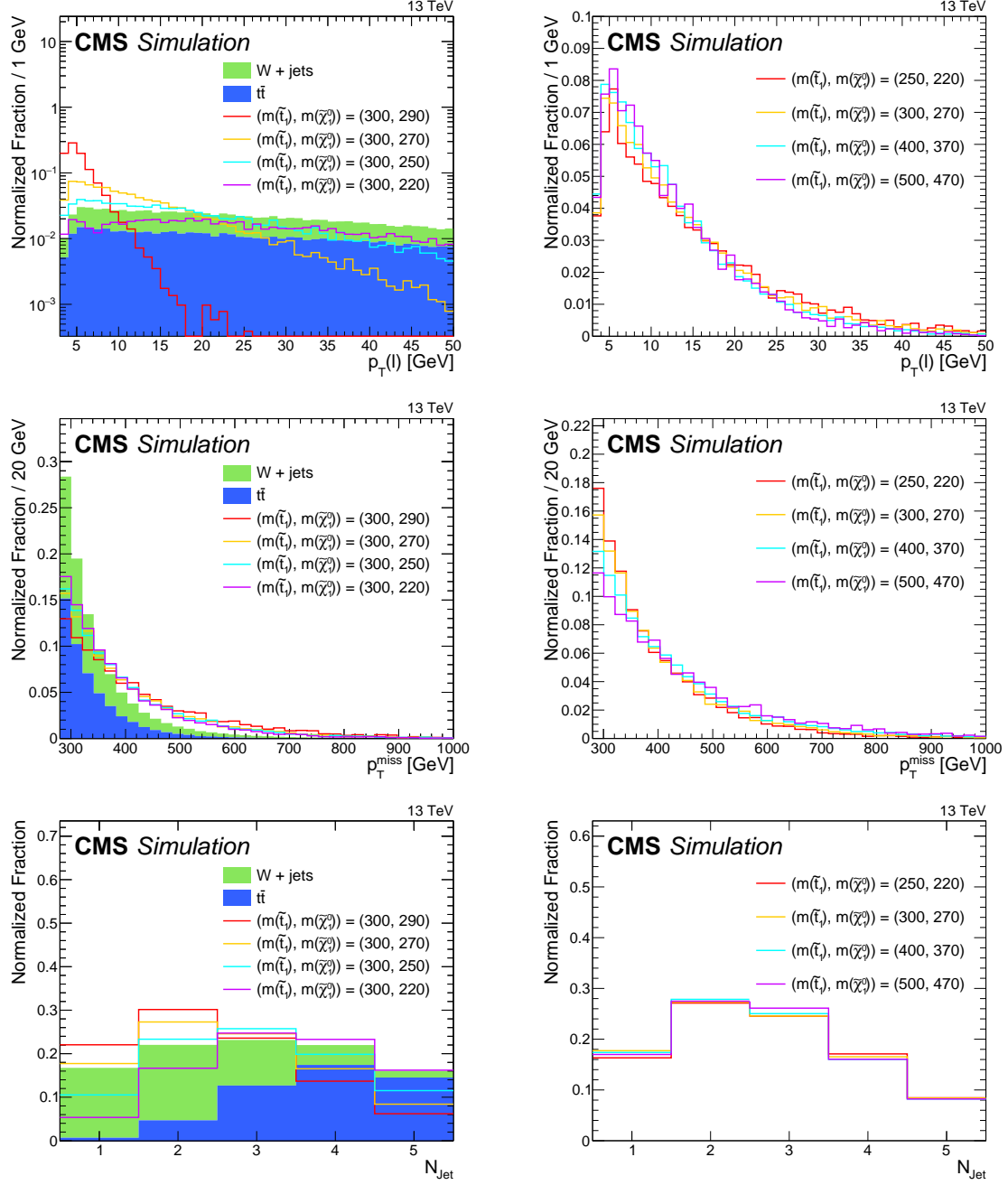
Figure 3: Simulated distributions of $p_T(\ell)$ (upper), p_T^{miss} (middle), and N_{jet}(lower) after the preselection. The W+jets and $t\bar{t}$ background distributions are shown as colored histograms, and the signal distributions by the solid lines. The total background distribution and the signal distributions are all normalized to unit area. On the left, the signal distributions are given for a top squark mass of 300 GeV and $\Delta m = 10$, 30, 50, and 80 GeV. On the right, the signal distributions are shown for four different $(m(\tilde{t}_1), m(\tilde{\chi}_1^0))$ values, all corresponding to the same $\Delta m = 30$ GeV.
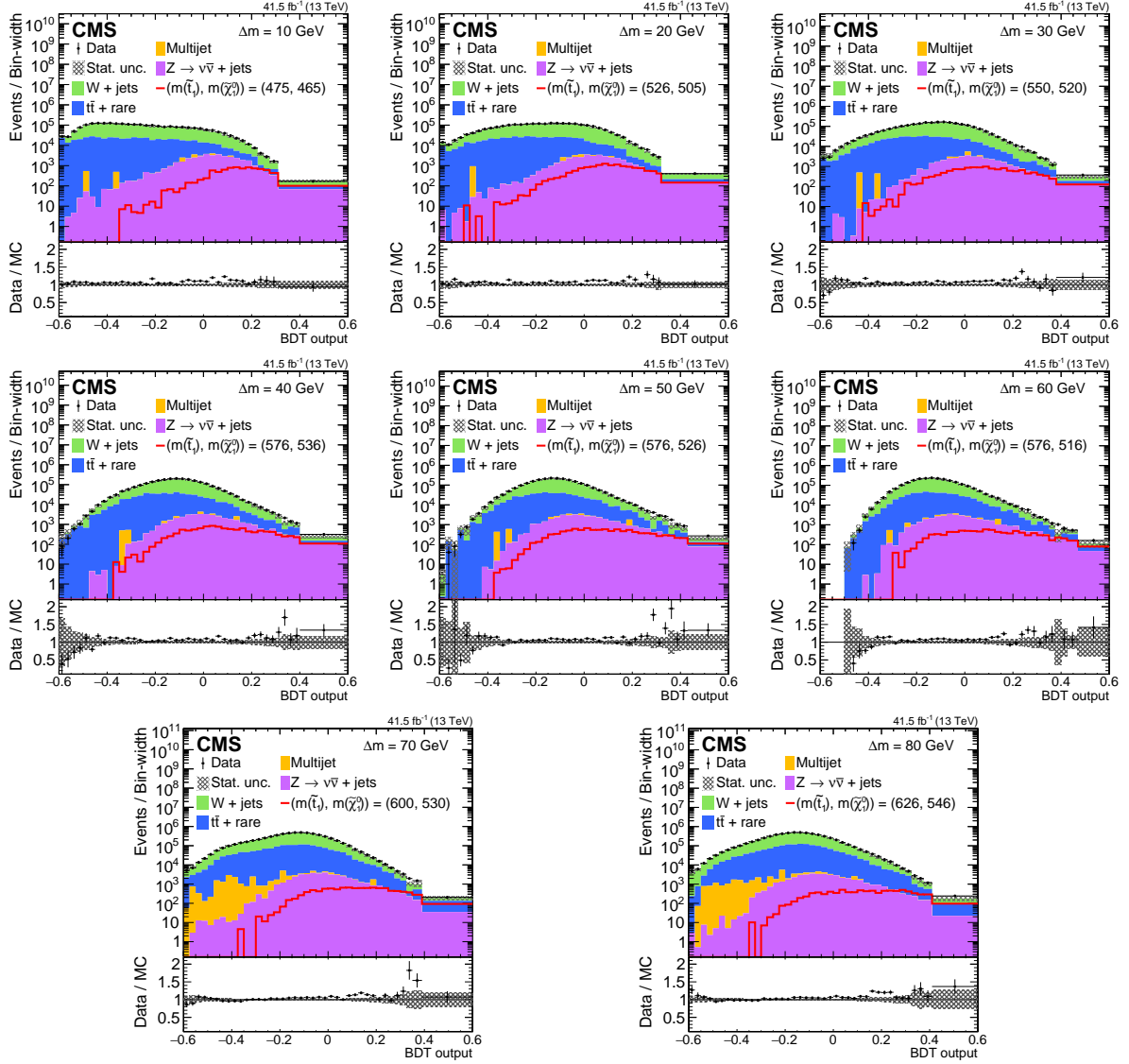
Figure 4: BDT output distributions from data (points) and simulation (colored histograms) after the preselection in 10 GeV steps of Δm from 10 (upper left) to 80 (lower right) GeV for the 2017 data. The last bin corresponds to the SR. The $t\bar{t}$ and rare backgrounds are represented together. For each Δm value, the predicted signal distribution is shown by the solid red line for a representative $(m(\widetilde{t}_1),\ m(\widetilde{\chi}_1^0))$ point, unstacked from the histograms. The lower panels show the ratio of the data to the sum of the background predictions, with the vertical bars and shaded area giving the statistical uncertainty in the data and the simulated background, respectively.
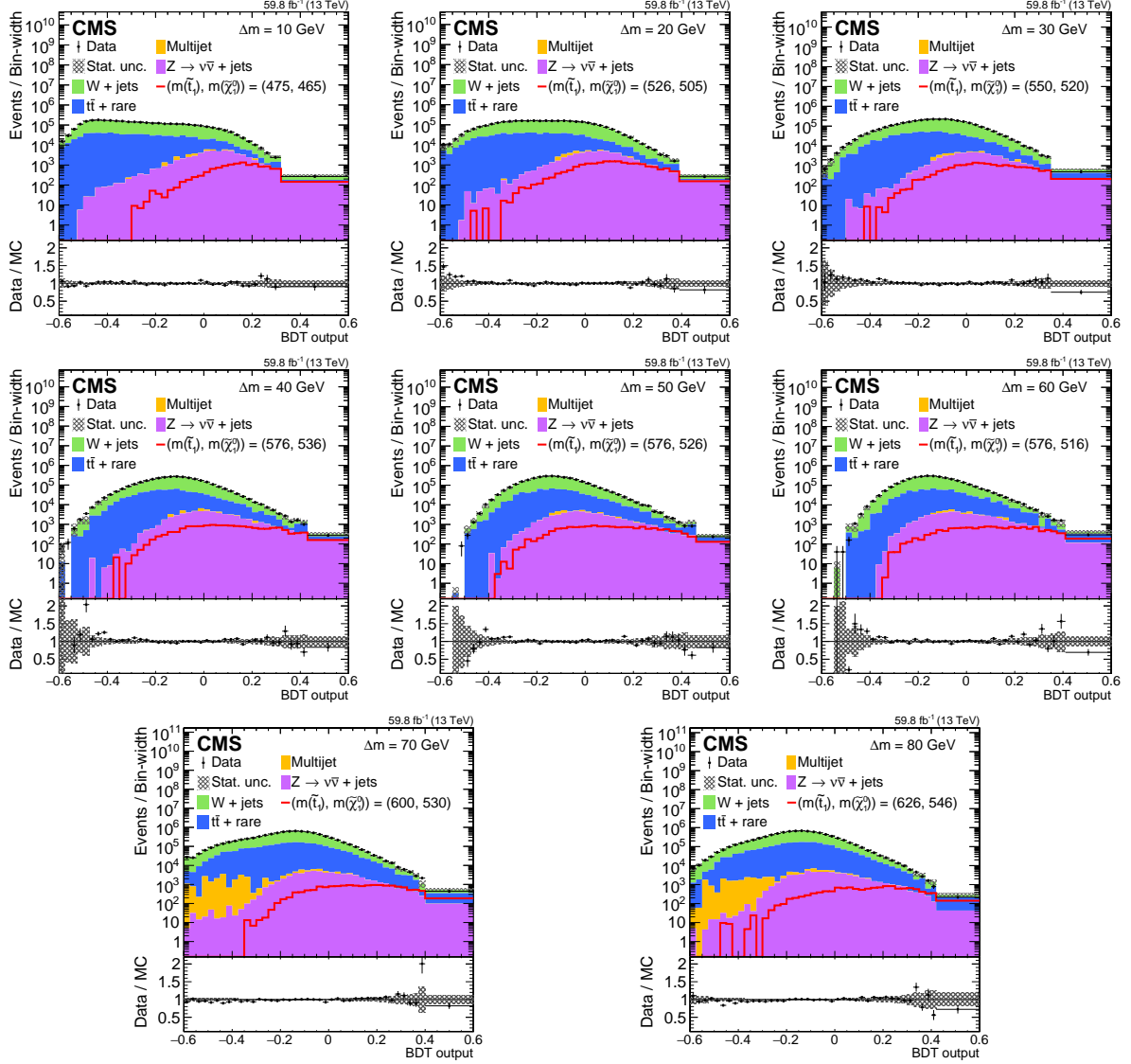
Figure 5: BDT output distributions from data (points) and simulation (colored histograms) after the preselection in 10 GeV steps of Δm from 10 (upper left) to 80 (lower right) GeV for the 2018 data. The last bin corresponds to the SR. The $t\bar{t}$ and rare backgrounds are represented together. For each Δm value, the predicted signal distribution is shown by the solid red line for a representative $(m(\tilde{t}_1), m(\tilde{\chi}_1^0))$ point, unstacked from the histograms. The lower panels show the ratio of the data to the sum of the background predictions, with the vertical bars and shaded area giving the statistical uncertainty in the data and the simulated background, respectively.

sources of background are estimated using data, as described in Sections 6.1 and 6.2. The background from rare SM processes, such as single top quark, diboson, DY, and $t\bar{t}X$ production, are estimated from simulation.

6.1 Nonprompt background

The nonprompt background is estimated from data using the "tight-to-loose" method [64]. The tight criteria correspond to the selection of the lepton as described in Section 4. The loose selection is defined by relaxing the requirement on the isolation variable to $I_{abs} < 20\,\mathrm{GeV}$ for $p_T(\ell) < 25\,\mathrm{GeV}$ and $I_{rel} < 0.8$ for $p_T(\ell) > 25\,\mathrm{GeV}$, and on the impact parameters to $|d_{xy}| < 0.1\,\mathrm{cm}$ and $|d_z| < 0.5\,\mathrm{cm}$. We call a lepton passing these requirements a loose lepton. The probability ϵ_{TL} for a loose lepton to pass the tight criteria is measured as a function of its p_T and η in a data CR that is largely dominated by multijet events and enriched in nonprompt leptons. For each SR, we define a side-band region with the same requirements, but where the lepton must pass the loose criteria while failing the tight ones ("L!T"). We denote the number of such events in data as $N^{L!T}(\mathrm{Data})$. From the data sample with a loose-not-tight lepton, we subtract the number of events $N_p^{L!T}(\mathrm{MC})$ from simulation where a vector boson or a top quark produce a prompt lepton. The predicted nonprompt yield Y_{np}^{SR} in each SR is obtained by weighting the resulting number of events by $\epsilon_{TL}/(1 - \epsilon_{TL})$:

$$Y_{np}^{SR} = \frac{\epsilon_{TL}}{1 - \epsilon_{TL}}[N^{L!T}(\mathrm{Data}) - N_p^{L!T}(\mathrm{MC})]. \tag{1}$$

6.2 Dominant prompt backgrounds

To estimate the prompt contributions from the W+jets and $t\bar{t}$ processes, we use a method based on the number of these background events observed in data CRs. The method uses the output of the BDT, and a transfer factor between the CR and the SR, obtained from simulation. This factor is the ratio of the number of predicted events in the SR, N_p^{SR}, to the one in the CR, N_p^{CR}. The estimated yield Y_p^{SR} of the dominant prompt background in the SR is then determined using:

$$Y_p^{SR}(X) = \frac{N_p^{SR}(X)}{N_p^{CR}(X)}\left[N^{CR}(\mathrm{Data}) - N_p^{CR}(\mathrm{Rare}) - Y_{np}^{CR}\right], \tag{2}$$

where X refers to the background process being estimated, either W+jets or $t\bar{t}$, and where the terms prompt and nonprompt refer to their definition as given at the beginning of Section 6. To obtain a data sample enriched in the backgrounds being estimated, a CR is defined by applying the preselection criteria, with the additional requirement BDT < 0. The number of such events is denoted as $N^{CR}(\mathrm{Data})$. To enrich the CR in W+jets or $t\bar{t}$ events, we require the number of loosely b-tagged jets to be zero, or the number of tightly b-tagged jets to be at least one, respectively, where loose and tight were discussed in Section 4 [57]. The purity of W+jets and $t\bar{t}$ processes in the corresponding CRs is approximately 93% and 78%, respectively. The level of signal contamination in the CR is well below 5%. The number $N_p^{CR}(\mathrm{Rare})$ of prompt lepton events from rare processes in the CR is estimated from simulation and subtracted from the number of data events. We also subtract the yield Y_{np}^{CR}, which is the predicted number of nonprompt background in the CR.

7 Summary of systematic uncertainties

Processes for which the absolute yield is predicted by simulation are subject to systematic uncertainties in the determination of the integrated luminosity, which is estimated year-by-year

with uncertainties in the 1.2–2.5% range [65, 66]. All simulated samples are subject to experimental uncertainties in the jet energy scale (JES) and jet energy resolution (JER). The uncertainties arising from miscalibration of the JES are estimated by varying the jet energy corrections up and down by one standard deviation of their uncertainties and propagating the effect to the calculation of $p_{\mathrm{T}}^{\mathrm{miss}}$. Differences in the JER between data and simulation are accounted for by smearing the momenta of jets in simulation. The uncertainties corresponding to the b tagging efficiencies and misidentification rates for tagging light-flavored quark or gluon jets as b jets have been evaluated for all simulated samples. The systematic uncertainties in the scale factors applied to the simulated samples for trigger and lepton efficiencies are taken into account. The uncertainty due to the simulation of pileup for simulated background processes is estimated by varying the inelastic pp cross section by 4.6% [67]. An uncertainty of 50% is assigned to the cross sections of all backgrounds whose yields are predicted from simulation.

The estimation of nonprompt backgrounds, as described in Section 6.1, depends on the tight-to-loose fraction ϵ_{TL}, which is sensitive to the flavor content of jets. The systematic uncertainty arising from this source in the measurement region is estimated by changing the b tagging requirement in the b veto to demand at least one b-tagged jet using the medium working point. The resulting uncertainty ranges from 3 to 90% from low to high lepton p_{T}, respectively. The method is also tested by repeating this procedure on the simulated event samples, where any variations in the background determination are considered as systematic uncertainties and added in quadrature to the aforementioned uncertainty.

The systematic uncertainties associated with the predictions of W+jets and $t\bar{t}$ processes are based on differences between the predicted number of events (obtained from Eq. (2)) and the observed number of data events in both VRs, as defined in Section 5.2, where the statistical uncertainty in the number of CR events is taken into account. The uncertainties are evaluated in the two VRs, and the larger value is used. Uncertainties in modeling the BDT output distribution, which can affect the background prediction, are assessed by comparing the ratio of the BDT output distributions for data to the background prediction in the CR with the ratio in the SR, for the two VRs. The estimations of the W+jets and $t\bar{t}$ backgrounds rely partially on the simulation and are therefore sensitive to theoretical uncertainties in the modeling of ISR. For the $t\bar{t}$ process, half of the ISR correction is assigned as the systematic uncertainty, which also applies to the simulated signal samples. For the W+jets process, the difference between the ISR-corrected and uncorrected simulation is taken as the systematic uncertainty.

Uncertainties from unknown higher-order theoretical effects are estimated through uncorrelated variations of the renormalization and factorization scales by factors of 0.5, 1, and 2 [68]. Finally, differences between the fast and the full GEANT4-based modelings of $p_{\mathrm{T}}^{\mathrm{miss}}$ are used as the corresponding systematic uncertainty and assigned to the signal yields. The statistical uncertainty in the signal simulation samples of 3 to 20% over the various SRs is included as a systematic uncertainty. The relative systematic uncertainties in the signal from the various sources, and the total relative systematic uncertainties in the W+jets, $t\bar{t}$, and nonprompt backgrounds, are given in Table 1 as ranges over the eight SRs.

To combine the results from the different data-taking years, we take as fully correlated those systematic uncertainties whose sources are exactly the same for the different years. This includes the uncertainty in the theoretical cross sections, pileup, JES, the reweighting of the W+jets sample, the renormalization and factorization scales, and the prediction of the W+jets, $t\bar{t}$, and nonprompt backgrounds. The systematic uncertainty in the integrated luminosity has multiple components and is thus considered as partially correlated between the years [19, 65, 66], as is the systematic uncertainty in the b tagging procedure.

Table 1: The relative systematic uncertainties in percent from the different sources in the signal and the total relative uncertainty in the W+jets, $t\bar{t}$, and nonprompt background predictions, shown separately for the 2017 and 2018 data analysis. The ranges given are across the eight SRs. The "—" symbol means that a given source of uncertainty is not applicable.

	2017		2018	
Source	Background	Signal	Background	Signal
Integrated luminosity	—	2.3	—	2.5
JES	0–2	3–9	0–2	5–10
JER	0–1	0–1	0–1	0–1
b tagging	0–1	0–6	0–1	0–1
Trigger	0–1	1	0–1	1
Lepton efficiency	0–1	0–1	0–1	0–1
Pileup	1–5	0–3	1–4	0–1
ISR ($t\bar{t}$ and signal)	0–1	0–5	0–1	0–5
ISR (W+jets)	0–4	—	0–4	—
Renorm./Fact. scales	0–7	0–1	0–10	0–1
p_T^{miss} modeling (FASTSIM)	—	0–2	—	0–2
W+jets total	2–6	—	4–9	—
$t\bar{t}$ total	1–5	—	2–7	—
Nonprompt lepton total	2–5	—	2–4	—

8 Results and interpretation

The observed and expected numbers of signal and background events from the 2017-18 data analysis for the eight values of Δm are given in Table 2 and shown in Figs. 6 and 7. The predictions and the associated uncertainties in these figures are given before the fit is performed [69–71]. There is good agreement between the observed and predicted numbers of events for all SRs. The largest difference is for $\Delta m = 10\,\text{GeV}$, where there are 1.1 and 2.9 standard deviations (local significance) excesses of signal events over the predicted background for the 2017 and 2018 data, respectively. The 2016 analysis had a similar excess for the same Δm value, corresponding to 0.7 standard deviations. None of these excesses is statistically significant, so we conclude that there is no evidence for direct top squark production.

The observed and expected number of events for each signal mass point and their corresponding uncertainties are converted into 95% confidence level (CL) upper limits on the $\widetilde{t}_1\overline{\widetilde{t}}_1$ production cross section in the $(m(\widetilde{t}_1),\ m(\widetilde{\chi}_1^0))$ plane. These are shown by the colored regions in Fig. 8 as a function of $m(\widetilde{t}_1)$ and Δm, where the color scale to the right of the figure gives the corresponding upper limit values. The limits are calculated according to the modified frequentist CL_s criterion [69–71]. A test statistic is defined as the likelihood ratio between the background-only and signal-plus-background hypotheses, and is used to set exclusion limits on the top squark pair production. The distributions of the test statistic are built using simulated experiments, where statistical uncertainties are modeled with Poisson distributions, and where all systematic uncertainties are modeled with a log-normal distribution. When interpreting the results, we assume a branching fraction of 100% for the four-body decay scenario. For the combined results of the three years, the largest excess in the data corresponds to 2.5 standard deviations (local significance) for the $\Delta m = 10\,\text{GeV}$ SR.

Using the measured upper limits on the top squark pair cross section and the theoretical predictions for the cross section, we determine the 95% CL lower limits on $m(\widetilde{t}_1)$ versus Δm. The solid black line and thick dotted red line in Fig. 8 give the resulting 95% CL observed and
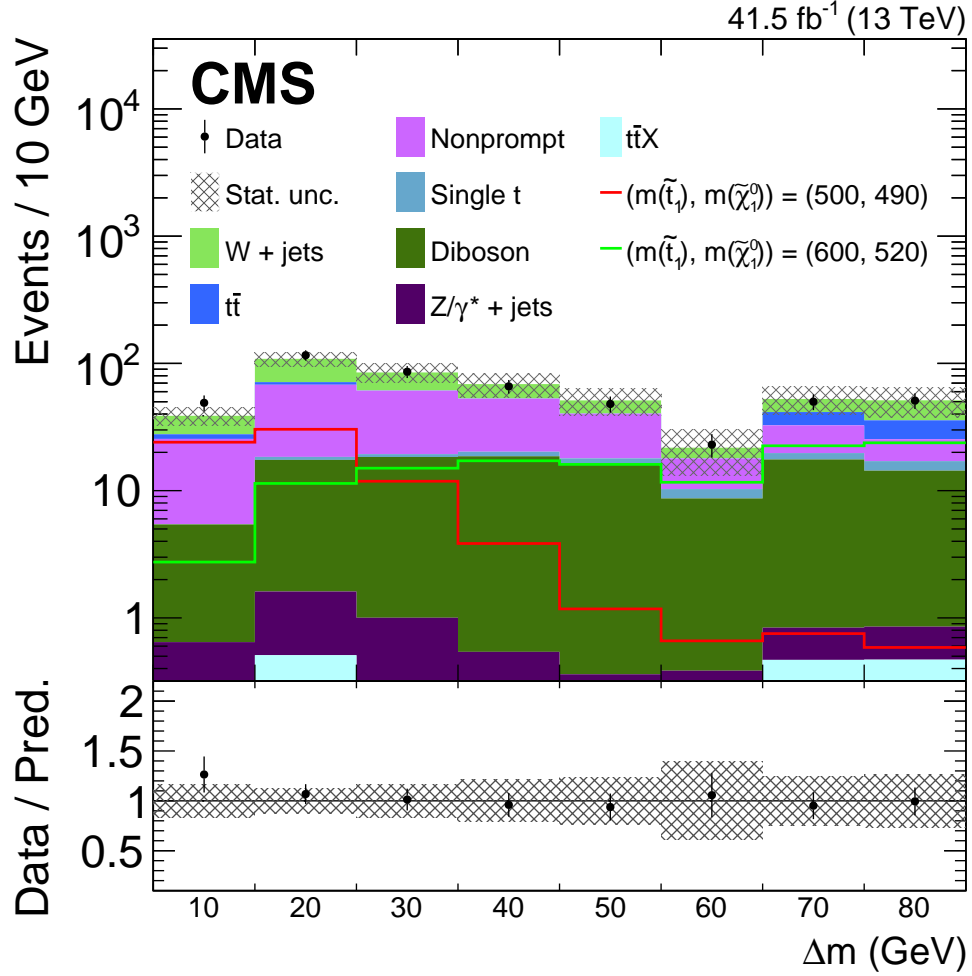
Figure 6: The observed yields in data (points) and the predicted background components (colored histograms) in the eight SRs for the 2017 data. The vertical bars on the points give the statistical uncertainty in the data. The hatched area shows the total uncertainty in the sum of the backgrounds. The expected yields for two signal points with $(m(\widetilde{t}_1), m(\widetilde{\chi}_1^0)) = (500, 490)$ and $(600, 520)$ GeV are also given by the lines, unstacked from the histograms. The lower panel shows the ratio of the number of observed events to the predicted total background. The vertical bars on the points give the statistical uncertainty in the ratio and the hatched area the systematic uncertainty.
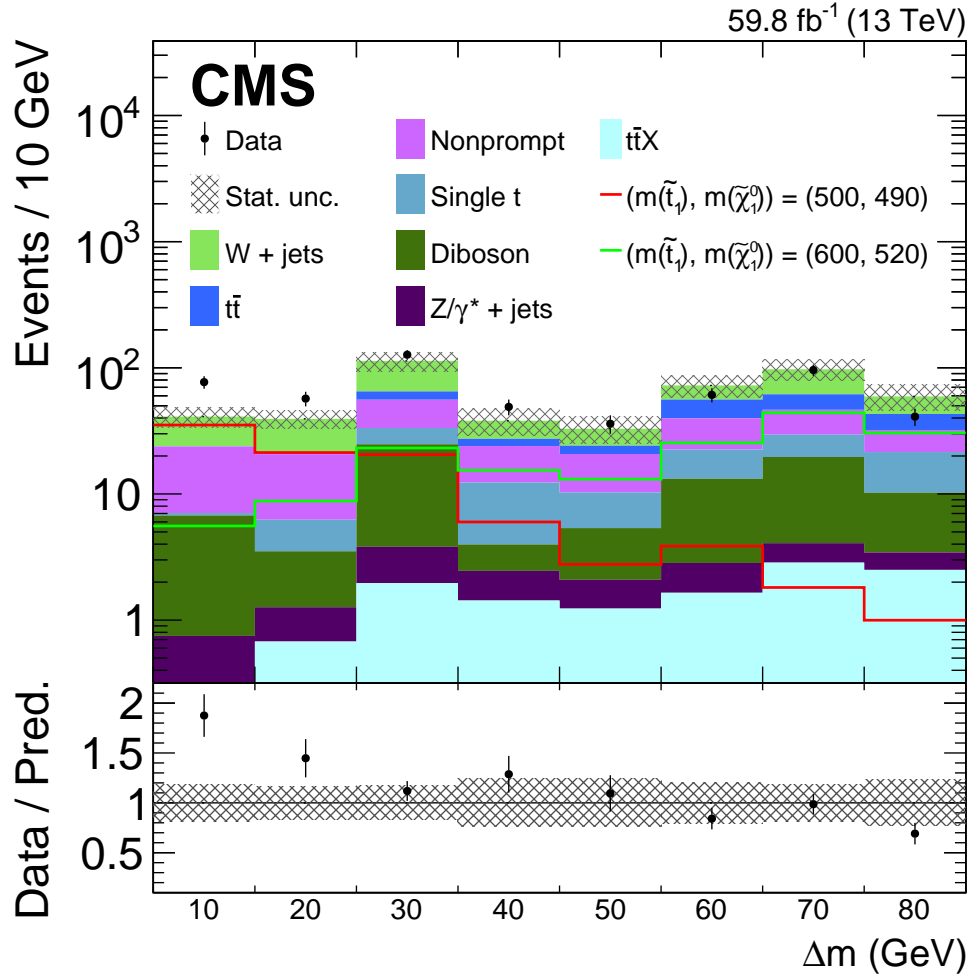
Figure 7: The observed yields in data (points) and the predicted background components (colored histograms) in the eight SRs for the 2018 data. The vertical bars on the points give the statistical uncertainty in the data. The hatched area shows the total uncertainty in the sum of the backgrounds. The expected yields for two signal points with $(m(\widetilde{t}_1), m(\widetilde{\chi}_1^0)) = (500, 490)$ and $(600, 520)$ GeV are also given by the lines, unstacked from the histograms. The lower panel shows the ratio of the number of observed events to the predicted total background. The vertical bars on the points give the statistical uncertainty in the ratio and the hatched area the systematic uncertainty.

Table 2: The predicted number of W+jets, $t\bar{t}$, nonprompt, and rare (N^{SR}(Rare)) background events and their sum (N^{SR}(Total)), in the eight SRs for the 2017 and 2018 data analysis. The first 3 predicted yields are derived from data, while the yields for the rare decay background come from simulation. The uncertainties shown are the quadratic sum of the statistical and systematic uncertainties given in Table 1 for background processes predicted from data, and the uncertainties in the cross section for the backgrounds predicted from simulation. The corresponding Δm and BDT output threshold values for each SR are displayed in the first and second columns, respectively, and the observed number of events in data is shown in the last column.

Year	Δm (GeV)	BDT >	Y_{p}^{SR}(W+jets)	Y_{p}^{SR}($t\bar{t}$)	Y_{np}^{SR}	N^{SR}(Rare)	N^{SR}(Total)	N^{SR}(Observed)
2017	10	0.31	11.0 ± 2.2	2.9 ± 2.9	20.1 ± 3.5	5.4 ± 3.7	38.8 ± 6.3	49
	20	0.32	37.4 ± 4.6	3.3 ± 5.2	49.6 ± 7.0	18.3 ± 9.2	109 ± 14	116
	30	0.38	23.8 ± 3.8	0.0 ± 7.2	41.7 ± 6.1	19.2 ± 9.9	85 ± 14	86
	40	0.40	15.9 ± 2.6	0.0 ± 8.1	32.6 ± 5.5	20 ± 10	69 ± 15	66
	50	0.43	10.9 ± 2.1	0.0 ± 6.7	22.3 ± 4.0	17.8 ± 9.1	51 ± 12	48
	60	0.47	3.9 ± 0.8	0.0 ± 6.2	7.6 ± 2.2	10.2 ± 5.4	21.8 ± 8.5	23
	70	0.39	11.1 ± 2.0	8.9 ± 7.6	12.9 ± 2.9	19.6 ± 9.7	53 ± 13	50
	80	0.41	15.6 ± 4.3	10.3 ± 9.7	8.3 ± 2.2	16.9 ± 8.2	51 ± 14	51
2018	10	0.32	17.3 ± 4.3	0.0 ± 2.4	16.7 ± 3.6	7.1 ± 4.5	41.1 ± 7.6	77
	20	0.39	18.4 ± 2.8	0.3 ± 3.1	14.5 ± 3.4	6.3 ± 3.5	39.4 ± 6.4	57
	30	0.35	48.5 ± 8.1	9.1 ± 9.4	22.5 ± 4.8	33 ± 14	114 ± 19	127
	40	0.43	10.7 ± 3.1	3.4 ± 4.5	11.7 ± 2.9	12.3 ± 6.7	38.1 ± 9.1	49
	50	0.46	8.7 ± 3.0	3.4 ± 4.5	10.5 ± 2.8	10.3 ± 5.2	32.9 ± 8.0	36
	60	0.41	16.5 ± 4.7	16.2 ± 8.8	17.3 ± 3.8	23 ± 10	73 ± 15	61
	70	0.40	35.7 ± 8.7	15.2 ± 8.6	16.9 ± 5.2	30 ± 12	97 ± 18	96
	80	0.42	16.3 ± 3.7	10.9 ± 7.8	10.7 ± 4.3	21.4 ± 9.8	59 ± 14	41

expected exclusion contours, respectively, on $m(\tilde{t}_1)$ as a function of Δm, obtained from combining the 2016, 2017, and 2018 data. The corresponding thin black lines in Fig. 8 represent the ± 1 standard deviation (σ_{theory}) variations in the limits due to the theoretical uncertainties in the case of the observed limits. The thin dashed red lines give the ± 1 and ± 2 standard deviation ($\sigma_{experiment}$) variations in the case of the expected limits, coming from the experimental uncertainties. The maximum sensitivity is reached for the highest Δm ($\Delta m \approx m(W)$), where top squark masses up to 700 GeV are excluded. At the lowest Δm value of 10 GeV covered by the search, the corresponding value is 480 GeV. The reduced sensitivity at lower Δm is explained by the lower transverse momentum spectrum of the decay products, as shown in Fig. 2, which results in a loss of acceptance.

Compared to the results of a similar analysis by the ATLAS Collaboration for the same decay mode and final state [20], the search presented here has comparable limits at intermediate and high Δm values. However, at low Δm, the excluded top squark mass is 120 GeV higher than the ATLAS limit. This is attributed to a more inclusive preselection criteria, where b tagging is not used, and where the discrimination between the signal and the dominating W+jets background is done by a multivariate analysis tool, whose performance is further enhanced by a BDT specifically trained for each Δm.

9 Summary

The results of a search for the direct pair production of top squarks in single-lepton final states are presented within a compressed scenario where R parity is conserved and the mass difference $\Delta m = m(\tilde{t}_1) - m(\tilde{\chi}_1^0)$ between the lightest top squark ($\tilde{t}_1$) and the lightest supersymmetric
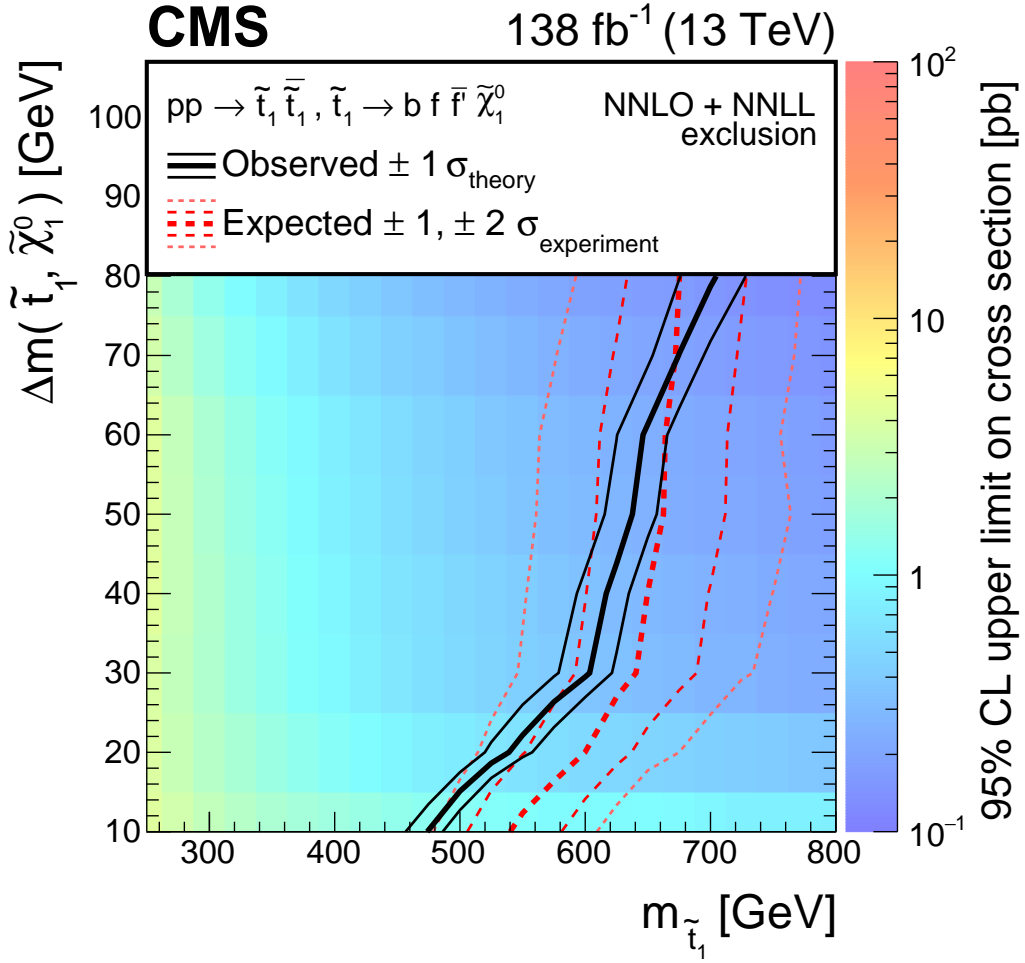
Figure 8: The 95% CL upper limits in the ($m(\tilde{t}_1)$, Δm) plane on the cross section for the production and four-body decay of the top squark using the combined 2016, 2017, and 2018 data. The color shading represents the observed upper limit for a given point in the plane, using the color scale to the right of the figure. The solid black and dashed red lines show the observed and expected 95% CL lower limits, respectively, on $m(\tilde{t}_1)$ as a function of Δm. The thick lines give the central values of the limits. The corresponding thin lines represent the ± 1 standard deviation (σ_{theory}) variations in the limits due to the theoretical uncertainties in the case of the observed limits, and ± 1 and 2 standard deviation ($\sigma_{experiment}$) variations due to the experimental uncertainties in the case of the expected limits.

particle, taken to be the lightest neutralino $\widetilde{\chi}_1^0$, does not exceed the W boson mass. The considered decay mode of the top squark is the prompt four-body decay to $b f \bar{f}' \widetilde{\chi}_1^0$, where the fermions in the final state f and $\bar{f}'$ represent a charged lepton and its neutrino for the decay products of one $\widetilde{t}_1$, and two quarks for the other top squark. The search is based on data collected from proton-proton collisions at $\sqrt{s} = 13\,\text{TeV}$, recorded with the CMS detector during the years 2016, 2017, and 2018, corresponding to an integrated luminosity of $138\,\text{fb}^{-1}$. Events are selected containing a single lepton (electron or muon), at least one high-momentum jet, and significant missing transverse momentum. The analysis is based on a multivariate tool specifically trained for different Δm regions, thus adapting the signal selection to the evolution of the kinematical variables as a function of $(m(\widetilde{t}_1),\ m(\widetilde{\chi}_1^0))$. The dominant background processes are W+jets, $t\bar{t}$, and events with nonprompt leptons, which are estimated using control regions in the data.

The observed number of events is consistent with the predicted standard model backgrounds in all signal regions. Upper limits are set at the 95% confidence level on the $\widetilde{t}_1\bar{\widetilde{t}}_1$ production cross section as a function of the $\widetilde{t}_1$ and $\widetilde{\chi}_1^0$ masses, within the context of a simplified model. Assuming a 100% branching fraction in the four-body decay mode, and computing the top squark pair production cross section at next-to-next-to-leading-order accuracy plus next-to-next-to-leading-logarithmic precision [42–48], the cross section upper limit is converted into a mass limit. The search excludes top squark masses up to 480 and 700 GeV at $\Delta m = 10$ and 80 GeV, respectively. The results summarized in this paper are among the best limits to date on the top squark pair production cross section, where the top squark decays via the four-body mode, and currently correspond to the most stringent limits for $\Delta m < 30\,\text{GeV}$.

References

[1] S. P. Martin, "A supersymmetry primer", *Adv. Ser. Direct. High Energy Phys.* **18** (1998) 1, `doi:10.1142/9789812839657_0001`, `arXiv:hep-ph/9709356`.

[2] J. Wess and B. Zumino, "Supergauge transformations in four dimensions", *Nucl. Phys. B* **70** (1974) 39, `doi:10.1016/0550-3213(74)90355-1`.

[3] H. P. Nilles, "Supersymmetry, supergravity and particle physics", *Phys. Rept.* **110** (1984) 1, `doi:10.1016/0370-1573(84)90008-5`.

[4] H. E. Haber and G. L. Kane, "The search for supersymmetry: Probing physics beyond the standard model", *Phys. Reports* **117** (1985) 75, `doi:10.1016/0370-1573(85)90051-1`.

[5] R. Barbieri, S. Ferrara, and C. A. Savoy, "Gauge models with spontaneously broken local supersymmetry", *Phys. Lett. B* **119** (1982) 343, `doi:10.1016/0370-2693(82)90685-2`.

[6] S. Dawson, E. Eichten, and C. Quigg, "Search for supersymmetric particles in hadron-hadron collisions", *Phys. Rev. D* **31** (1985) 1581, `doi:10.1103/PhysRevD.31.1581`.

[7] ATLAS Collaboration, "Observation of a new particle in the search for the standard model Higgs boson with the ATLAS detector at the LHC", *Phys. Lett. B* **716** (2012) 1, `doi:10.1016/j.physletb.2012.08.020`, `arXiv:1207.7214`.

[8] CMS Collaboration, "Observation of a new boson at a mass of 125 GeV with the CMS experiment at the LHC", *Phys. Lett. B* **716** (2012) 30, `doi:10.1016/j.physletb.2012.08.021`, `arXiv:1207.7235`.

[9] CMS Collaboration, "Observation of a new boson with mass near 125 GeV in pp collisions at $\sqrt{s}$ = 7 and 8 TeV", *JHEP* **06** (2013) 081, `doi:10.1007/JHEP06(2013)081`, `arXiv:1303.4571`.

[10] G. R. Farrar and P. Fayet, "Phenomenology of the production, decay, and detection of new hadronic states associated with supersymmetry", *Phys. Lett. B* **76** (1978) 575, `doi:10.1016/0370-2693(78)90858-4`.

[11] C. Balázs, M. Carena, and C. E. M. Wagner, "Dark matter, light stops and electroweak baryogenesis", *Phys. Rev. D* **70** (2004) 015007, `doi:10.1103/PhysRevD.70.015007`, `arXiv:hep-ph/0403224`.

[12] T. Cohen et al., "SUSY simplified models at 14, 33, and 100 TeV proton colliders", *JHEP* **04** (2014) 117, `doi:10.1007/JHEP04(2014)117`, `arXiv:1311.6480`.

[13] N. Arkani-Hamed et al., "MARMOSET: the path from LHC data to the new standard model via on-shell effective theories", 2007. `arXiv:hep-ph/0703088.`.

[14] J. Alwall, P. C. Schuster, and N. Toro, "Simplified models for a first characterization of new physics at the LHC", *Phys. Rev. D* **79** (2009) 075020, `doi:10.1103/PhysRevD.79.075020`, `arXiv:0810.3921`.

[15] J. Alwall, M.-P. Le, M. Lisanti, and J. G. Wacker, "Model-independent jets plus missing energy searches", *Phys. Rev. D* **79** (2009) 015005, `doi:10.1103/PhysRevD.79.015005`, `arXiv:0809.3264`.

[16] D. Alves et al., "Simplified models for LHC new physics searches", *J. Phys. G* **39** (2012) 105005, `doi:10.1088/0954-3899/39/10/105005`, `arXiv:1105.2838`.

[17] CMS Collaboration, "Interpretation of searches for supersymmetry with simplified models", *Phys. Rev. D* **88** (2013) 052017, `doi:10.1103/PhysRevD.88.052017`, `arXiv:1301.2175`.

[18] CMS Collaboration, "Search for top squarks decaying via four-body or chargino-mediated modes in single-lepton final states in proton-proton collisions at $\sqrt{s}$ = 13 TeV", *JHEP* **09** (2018) 065, `doi:10.1007/JHEP09(2018)065`, `arXiv:1805.05784`.

[19] CMS Collaboration, "Precision luminosity measurement in proton-proton collisions at $\sqrt{s} = 13$ TeV in 2015 and 2016 at CMS", *Eur. Phys. J. C* **81** (2021) 800, `doi:10.1140/epjc/s10052-021-09538-2`, `arXiv:2104.01927`.

[20] ATLAS Collaboration, "Search for new phenomena with top quark pairs in final states with one lepton, jets, and missing transverse momentum in pp collisions at $\sqrt{s}$ = 13 TeV with the ATLAS detector", *JHEP* **04** (2021) 174, `doi:10.1007/JHEP04(2021)174`, `arXiv:2012.03799`.

[21] HEPData record for this analysis, 2022. `doi:10.17182/hepdata.135455`.

[22] CMS Collaboration, "The CMS experiment at the CERN LHC", *JINST* **3** (2008) S08004, `doi:10.1088/1748-0221/3/08/S08004`.

[23] CMS Collaboration, "Performance of the CMS Level-1 trigger in proton-proton collisions at $\sqrt{s} = 13\,\text{TeV}$", *JINST* **15** (2020) P10017, `doi:10.1088/1748-0221/15/10/P10017`, `arXiv:2006.10165`.

[24] CMS Collaboration, "The CMS trigger system", *JINST* **12** (2017) P01020, `doi:10.1088/1748-0221/12/01/P01020`, `arXiv:1609.02366`.

[25] CMS Collaboration, "Electron and photon reconstruction and identification with the CMS experiment at the CERN LHC", *JINST* **16** (2021) P05014, `doi:10.1088/1748-0221/16/05/P05014`, `arXiv:2012.06888`.

[26] CMS Collaboration, "Performance of the CMS muon detector and muon reconstruction with proton-proton collisions at $\sqrt{s} = 13\,\text{TeV}$", *JINST* **13** (2018) P06015, `doi:10.1088/1748-0221/13/06/P06015`, `arXiv:1804.04528`.

[27] CMS Collaboration, "Description and performance of track and primary-vertex reconstruction with the CMS tracker", *JINST* **9** (2014) P10009, `doi:10.1088/1748-0221/9/10/P10009`, `arXiv:1405.6569`.

[28] J. Alwall et al., "The automated computation of tree-level and next-to-leading order differential cross sections, and their matching to parton shower simulations", *JHEP* **07** (2014) 079, `doi:10.1007/JHEP07(2014)079`, `arXiv:1405.0301`.

[29] P. Nason, "A new method for combining NLO QCD with shower Monte Carlo algorithms", *JHEP* **11** (2004) 040, `doi:10.1088/1126-6708/2004/11/040`, `arXiv:hep-ph/0409146`.

[30] S. Frixione, P. Nason, and C. Oleari, "Matching NLO QCD computations with parton shower simulations: the POWHEG method", *JHEP* **11** (2007) 070, `doi:10.1088/1126-6708/2007/11/070`, `arXiv:0709.2092`.

[31] S. Alioli, P. Nason, C. Oleari, and E. Re, "A general framework for implementing NLO calculations in shower Monte Carlo programs: the POWHEG BOX", *JHEP* **06** (2010) 043, `doi:10.1007/JHEP06(2010)043`, `arXiv:1002.2581`.

[32] S. Alioli, P. Nason, C. Oleari, and E. Re, "NLO single-top production matched with shower in POWHEG: *s*- and *t*-channel contributions", *JHEP* **09** (2009) 111, `doi:10.1088/1126-6708/2009/09/111`, `arXiv:0907.4076`. [Erratum: `doi:10.1007/JHEP02(2010)011`].

[33] E. Re, "Single-top Wt-channel production matched with parton showers using the POWHEG method", *Eur. Phys. J. C* **71** (2011) 1547, `doi:10.1140/epjc/s10052-011-1547-z`, `arXiv:1009.2450`.

[34] T. Melia, P. Nason, R. Röntsch, and G. Zanderighi, "W^+W^-, WZ and ZZ production in the POWHEG BOX", *JHEP* **11** (2011) 078, `doi:10.1007/JHEP11(2011)078`, `arXiv:1107.5051`.

[35] P. Nason and G. Zanderighi, "W^+W^-, WZ and ZZ production in the POWHEG-BOX-V2", *Eur. Phys. J. C* **74** (2014) 2702, `doi:10.1140/epjc/s10052-013-2702-5`, `arXiv:1311.1365`.

[36] H. B. Hartanto, B. Jäger, L. Reina, and D. Wackeroth, "Higgs boson production in association with top quarks in the POWHEG BOX", *Phys. Rev. D* **91** (2015) 094003, `doi:10.1103/PhysRevD.91.094003`, `arXiv:1501.04498`.

[37] NNPDF Collaboration, "Parton distributions from high-precision collider data", *Eur. Phys. J. C* **77** (2017) 663, `doi:10.1140/epjc/s10052-017-5199-5`, `arXiv:1706.00428`.

[38] R. Frederix and S. Frixione, "Merging meets matching in MC@NLO", *JHEP* **12** (2012) 061, `doi:10.1007/JHEP12(2012)061`, `arXiv:1209.6215`.

[39] T. Sjöstrand et al., "An introduction to PYTHIA 8.2", *Comput. Phys. Commun.* **191** (2015) 159, `doi:10.1016/j.cpc.2015.01.024`, `arXiv:1410.3012`.

[40] CMS Collaboration, "Extraction and validation of a new set of CMS PYTHIA 8 tunes from underlying-event measurements", *Eur. Phys. J. C* **80** (2020) 4, `doi:10.1140/epjc/s10052-019-7499-4`, `arXiv:1903.12179`.

[41] GEANT4 Collaboration, "GEANT4 — a simulation toolkit", *Nucl. Instrum. Meth. A* **506** (2003) 250, `doi:10.1016/S0168-9002(03)01368-8`.

[42] W. Beenakker, R. Höpker, and M. Spira, "PROSPINO: A program for the production of supersymmetric particles in next-to-leading order QCD", 1996. `arXiv:hep-ph/9611232`.

[43] C. Borschensky et al., "Squark and gluino production cross sections in pp collisions at $\sqrt{s}$ = 13, 14, 33 and 100 TeV", *Eur. Phys. J. C* **74** (2014) 3174, `doi:10.1140/epjc/s10052-014-3174-y`, `arXiv:1407.5066`.

[44] W. Beenakker, R. Höpker, M. Spira, and P. M. Zerwas, "Squark and gluino production at hadron colliders", *Nucl. Phys. B* **492** (1997) 51, `doi:10.1016/S0550-3213(97)80027-2`, `arXiv:hep-ph/9610490`.

[45] A. Kulesza and L. Motyka, "Threshold resummation for squark-antisquark and gluino-pair production at the LHC", *Phys. Rev. Lett.* **102** (2009) 111802, `doi:10.1103/PhysRevLett.102.11802`, `arXiv:hep-ph/0807.2405`.

[46] A. Kulesza and L. Motyka, "Soft gluon resummation for the production of gluino-gluino and squark-antisquark pairs at the LHC", *Phys. Rev. D* **80** (2009) 095004, `doi:10.1103/PhysRevD.80.095004`, `arXiv:hep-ph/0905.4749`.

[47] W. Beenakker et al., "Soft-gluon resummation for squark and gluino hadroproduction", *JHEP* **12** (2009) 41, `doi:10.1088/1126-6708/2009/12/041`, `arXiv:hep-ph/0909.4418`.

[48] W. Beenakker et al., "Squark and gluino production", *Int. J. Mod. Phys. A* **26** (2011) 2637, `doi:10.1142/S0217751X11053560`, `arXiv:hep-ph/1105.1110`.

[49] S. Abdullin et al., "The fast simulation of the CMS detector at LHC", *J. Phys. Conf. Ser.* **331** (2011) 032049, `doi:10.1088/1742-6596/331/3/032049`.

[50] A. Giammanco, "The fast simulation of the CMS experiment", *J. Phys. Conf. Ser.* **513** (2014) 022012, `doi:10.1088/1742-6596/513/2/022012`.

[51] CMS Collaboration, "Particle-flow reconstruction and global event description with the CMS detector", *JINST* **12** (2017) P10003, `doi:10.1088/1748-0221/12/10/P10003`, `arXiv:1706.04965`.

[52] CMS Collaboration, "Technical proposal for the Phase-II upgrade of the Compact Muon Solenoid", CMS Technical Proposal CERN-LHCC-2015-010, CMS-TDR-15-02, 2015.

[53] M. Cacciari, G. P. Salam, and G. Soyez, "The anti-k_T jet clustering algorithm", *JHEP* **04** (2008) 063, `doi:10.1088/1126-6708/2008/04/063`, `arXiv:0802.1189`.

[54] M. Cacciari, G. P. Salam, and G. Soyez, "FastJet user manual", *Eur. Phys. J. C* **72** (2012) 1896, `doi:10.1140/epjc/s10052-012-1896-2`, `arXiv:1111.6097`.

[55] CMS Collaboration, "Jet energy scale and resolution in the CMS experiment in pp collisions at 8 TeV", *JINST* **12** (2017) P02014, `doi:10.1088/1748-0221/12/02/P02014`, `arXiv:1607.03663`.

[56] CMS Collaboration, "Identification of heavy-flavour jets with the CMS detector in pp collisions at 13 TeV", *JINST* **13** (2018) P05011, `doi:10.1088/1748-0221/13/05/P05011`, `arXiv:1712.07158`.

[57] CMS Collaboration, "Performance of the DeepJet b tagging algorithm using 41.9 fb^{-1} of data from proton-proton collisions at 13 TeV with Phase 1 CMS detector", CMS Detector Performance Summary CMS-DP-2018-058, 2018.

[58] CMS Collaboration, "Performance of missing transverse momentum reconstruction in proton-proton collisions at $\sqrt{s} = 13$ TeV using the CMS detector", *JINST* **14** (2019) P07004, `doi:10.1088/1748-0221/14/07/P07004`, `arXiv:1903.06078`.

[59] CMS Collaboration, "Search for supersymmetry in pp collisions at $\sqrt{s} = 13$ TeV in the single-lepton final state using the sum of masses of large-radius jets", *JHEP* **08** (2016) 122, `doi:10.1007/JHEP08(2016)122`, `arXiv:1605.04608`.

[60] K. Rehermann and B. Tweedie, "Efficient identification of boosted semileptonic top quarks at the LHC", *JHEP* **03** (2011) 059, `doi:10.1007/JHEP03(2011)059`, `arXiv:1007.2221`.

[61] L. Rokach and O. Maimon, "Data mining with decision trees: theory and applications". World Scientific Pub. Co. Inc., 2008. ISBN 978-981-277-171-1.

[62] A. Hocker et al., "TMVA - toolkit for multivariate data analysis", *PoS* **ACAT** (2007) 040, `doi:10.48550/ARXIV.PHYSICS/0703039`, `arXiv:physics/0703039`.

[63] G. Cowan, K. Cranmer, E. Gross, and O. Vitells, "Asymptotic formulae for likelihood-based tests of new physics", *Eur. Phys. J. C* **71** (2011) 1554, `doi:10.1140/epjc/s10052-011-1554-0`, `arXiv:1007.1727`. [Erratum: `doi:10.1140/epjc/s10052-013-2501-z`].

[64] CMS Collaboration, "Search for new physics in same-sign dilepton events in proton-proton collisions at $\sqrt{s} = 13$ TeV", *Eur. Phys. J. C* **76** (2016) 439, `doi:10.1140/epjc/s10052-016-4261-z`, `arXiv:1605.03171`.

[65] CMS Collaboration, "CMS luminosity measurement for the 2017 data-taking period at $\sqrt{s} = 13$ TeV", CMS Physics Analysis Summary CMS-PAS-LUM-17-004, 2018.

[66] CMS Collaboration, "CMS luminosity measurement for the 2018 data-taking period at $\sqrt{s} = 13$ TeV", CMS Physics Analysis Summary CMS-PAS-LUM-18-002, 2019.

[67] CMS Collaboration, "Measurement of the inelastic proton-proton cross section at $\sqrt{s} = 13\,\text{TeV}$", *JHEP* **07** (2018) 161, `doi:10.1007/JHEP07(2018)161`, `arXiv:1802.02613`.

[68] A. Kalogeropoulos and J. Alwall, "The SysCalc code: A tool to derive theoretical systematic uncertainties", 2018. `arXiv:hep-ph/1801.08401`.

[69] T. Junk, "Confidence level computation for combining searches with small statistics", *Nucl. Instrum. Meth. A* **434** (1999) 435, `doi:10.1016/S0168-9002(99)00498-2`, `arXiv:hep-ex/9902006`.

[70] A. L. Read, "Presentation of search results: the CL_s technique", *J. Phys. G* **28** (2002) 2693, `doi:10.1088/0954-3899/28/10/313`.

[71] ATLAS and CMS Collaborations, LHC Higgs Combination Group, "Procedure for the LHC Higgs boson search combination in summer 2011", Technical Report ATL-PHYS-PUB/2011-11, CMS NOTE 2011/005, CERN, 2011.